Egypt. J. Chem. **Vol. 67** No. 3 pp. 457- 466 (2024)

Egyptian Journal of Chemistry

http://ejchem.journals.ekb.eg/

Purification of Water Contaminated with Heavy Metals, Exemplified by Lead Cations, Utilizing $Fe_2O_3@Al_2O_3$ Nanocomposites

Fatima A. Adam

Chemistry Department, Faculty of Science, Imam Mohammad Ibn Saud Islamic University (IMSIU), PO Box 90905, Riyadh, 11623, KSA

Abstract

The poisoning of natural water resources by waste discharge is a significant problem, and the search for a solution to a problem of this magnitude is a matter of concern on a global scale. Novel $Fe_2O_3@Al_2O_3$ nanocomposite was synthesized via a simple, low cost, green, and eco-friendly method utilizing glucose as a capping material. Transmission electron microscopy (TEM) results for the synthesized $Fe_2O_3@Al_2O_3$ revealed that the particle size is ranging between 3.5 and 13.9 nm. The sorbent possessed a specific surface area of 113.46 m^2 g^{-1} and was tested for removing heavy metals from water, exemplified by Pb^{2+}. $Fe_2O_3@Al_2O_3$ was proven to be an excellent sorbent for Pb^{2+}, with a qt value of 246.4 mg g^{-1} for a 2.0 h equilibrium time. The Pb^{2+} removal fitted a pseudo-second order (PSO) model, and the Pb^{2+} sorption onto $Fe_2O_3@Al_2O_3$ was controlled via a liquid-film diffusion model (LFM), which implied an excellent sorbent–sorbate affinity. The equilibrium studies revealed a better agreement of Pb^{2+} sorption with the Freundlich isotherm model (FIM), while the thermodynamic results indicated spontaneous endothermic physisorption. $Fe_2O_3@Al_2O_3$ showed an average efficiency of 96.8% in treated seawater (SW) and groundwater (GW) spiked with Pb^{2+}, and the sorbent activity after four cycles was 94.2% of its original efficiency, with an RSD of 5.19

Keywords: aluminum oxide; iron(III) oxide; nanocomposite; adsorption; water treatment; lead

1. Introduction

Research should focus on solving the global problem of the ongoing poisoning of natural water supplies. Toxic chemicals and other pollutants in the water supply pose a severe risk to human health worldwide [1]. This serious problem directly results from the widespread practice of discharging industrial waste into water supplies, which has increased dramatically in recent decades [2-5]. Organic colors, medicinal chemicals, and heavy metals contaminate industrial effluents [6]. Heavy metals are those with densities >5 g mL^{-1} and they represent a severe environmental and human-health threats. Industrial activities generate massive quantities of heavy-metal-contaminated wastewater. For example, manufacturing ammunition, batteries, pigments, and electroplating results in significant amounts of lead (Pb) contamination [7, 8]. Polluted effluents eventually reach local water bodies, negatively impacting aquatic life and the surrounding ecosystem [9]. Pb^{2+} accumulates in the food chain, causing harmful effects on people, plants, and animal. When evaluating the relative toxicity of heavy metals, Pb stands out as the most significant [10], with the worst-case scenario being entry into the human body directly through water supplies. The World Health Organization (WHO) has set 10 ppb as the maximum allowed Pb^{2+} concentration in drinking water [11]. Brain damage, kidney damage, anemia, malaise, and anorexia are some of the issues brought on by Pb-contaminated drinking water [12]. Water contaminants are treated and reduced using membranes, flocculation, chemical oxidation, ion exchange, and other techniques [13-21]. However, these methods have considerable challenges, such as being ineffective or expensive [22-24]. As nanoscience has developed, researchers have examined photodegradation and adsorption as effective water purification methods. Adsorption is a better solution than photodegradation, which might release toxic fragments and is inappropriate for treating heavy metal pollution [25-28]. Several sorbents perform well in removing heavy metals, with the benefits over photodegradation including minimal energy use and no release of hazardous compounds [29]. Al_2O_3 has long been recognized as an ideal bed stabilizer for metal oxide catalysts and

*Corresponding author e-mail: leno.ali20789@gmail.com.;(Fatima A. Adam).
Receive Date: 26 August 2023 Revise Date: 20 September 2023 Accept Date: 01 October 2023
DOI: 10.21608/EJCHEM.2023.231639.8496

an adsorbent in chromatography. It has attracted interest as a sorbent due to its high surface area and the presence of both basic and acidic functional groups [30]. For this reason, pure and composite Al_2O_3 continue to interest and be synthesized by scientists [31-36]. Researchers have studied nanocomposite synthesis, doping them with metal oxides, polymers, and ceramics to create superior sorbents with unique characteristics. Because doping materials affect the aggregation of the produced nanomaterial, their use significantly impacts the molecular structure [37]. Metal oxide deposition can increase the surface area and the number of hydroxyl groups on doped materials, improving their performance [38-40]. Researchers have considered the application of Fe_2O_3 materials in catalytic applications, including water treatment [41-43].

This study aims to use a new simple, cheap and ecofriendly method to prepare Fe_2O_3-doped Al_2O_3 (Fe_2O_3@Al_2O_3) nanocomposite. Glucose sugar was used as a capping material to prevent the formation of large particles. This composite would be characterized via FTIR, XRD, SEM, TEM and EDX analysis to confirm the successful preparation method. The synthesized Fe_2O_3@Al_2O_3 nanocomposite was used in the elimination of Pb^{2+} from aquas solution and contaminated water samples and the optimum conditions were studied in detail.

2. Experimental

2.1. Materials

Ferric chloride hexahydrate ($FeCl_3.6H_2O$, 99%), lead nitrate ($Pb(NO_3)_2$), and aluminum trichloride hexahydrate ($AlCl_3.6H_2O$, 99%) were obtained from LOBA CHEMIE (Mumbai, India). D-(+)-Glucose monohydrate ($C6H_{12}O_6.H_2O$; GL) was obtained from Riedel-de Haen (Germany).

2.2. Synthesis of Fe_2O_3@Al_2O_3 nanocomposites

In 100 ml of distilled water, we dissolved 22.41 g of $AlCl_3.6H_2O$ and 1.13 g of $FeCl_3.6H_2O$. Then, 10.0 g of GL was added to the mixture. Finally, the mixture was heated at 350 °C until the GL was carbonized. The powdered solid was placed in a porcelain dish and calcined in an oven at 1000 °C for 3 hours with a heating rate 80°C/min.

2.3. Characterization of Fe_2O_3@Al_2O_3 nanocomposites

Scanning electron microscopy and energy dispersive X-ray spectroscopy (SEM-EDS) were used to examine the fabricated nanomaterial's surface morphology (JSM-IT500HR, from JEOL USA). Transmission electron microscopy was utilized to investigate morphology in minute detail (JEM 1400, from JEOL USA). Fourier transform infrared (FTIR) spectrophotometry was used to analyze the bonding and functional groups (Shimadzu IR-tracer-100, Japan). A micromeritics surface analyzer was utilized to examine the surface properties (ASAP 2020, USA). Powder X-ray diffractometry was used to check the purity and crystallinity of the nanocomposite (Bruker, D8-Advance; Billerica, MA, USA).

2.4. Adsorption of Pb^{2+} on Fe_2O_3@Al_2O_3 nanocomposites

Fe_2O_3@Al_2O_3's efficacy in removing Pb^{2+} from polluted water was studied via a batch experiment method. The influence of the contact time was investigated by mixing 60 mg of Fe_2O_3@Al_2O_3 into 120 mL of Pb^{2+} solution (60 mg L^{-1}). The Pb^{2+} concentration was determined on a filtered portion, analyzed using an inductively coupled plasma atomic emission spectrophotometer (ICP-AES; SPECTRO GENESIS). The adsorption capacity (qt, mg g^{-1}) was calculated for each time point using Equation (1). The data were also used to examine the Pb^{2+} adsorption kinetics. The sorption rate was investigated using pseudo-first-order (PFO) and pseudo-second-order (PSO) kinetics models (Equations (2) and (3)). Additionally, the intra-particle and liquid-film diffusion models (IPM and LFM) were used to determine the mechanism regulating the adsorption (Equations (4) and (5)).

$$q_t = \frac{(C_0 - C_t)\,V}{M} \quad (1)$$

$$\ln(q_e - q_t) = \ln(q_e) - kt \quad (2)$$

$$\frac{1}{q_t} = \frac{1}{k_2 q_e^2\, t} + \frac{1}{q_e} \quad (3)$$

$$q_t = K_{Ip} * t^{\frac{1}{2}} + C_i \quad (4)$$

$$\ln(1 - F) = -K_{Lf} * t \quad (5)$$

C_0 and C_t (mg L^{-1}) represent the initial and final Pb^{2+} concentrations; V (L) and M (g) denote the volume of the Pb^{2+} solution and mass of the sorbent, respectively; k_1 (min^{-1}) represents the FOM rate constant; k_2 (g mg^{-1} min^{-1}) represents the SOM rate constant; K_{Ip} (mg g^{-1} $min^{-0.5}$) and K_{Lf} (min) represent the IM and LDM constants, respectively. Additionally, the Fe_2O_3@Al_2O_3 was subjected to Pb2+ adsorption tests in a pH-changing solution series; the 60 mg L^{-1} Pb^{2+} solution was altered to a pH between 2.0 and 10.0. A volume of 25 ml of the solution and 10 mg of Fe_2O_3@Al_2O_3 were shaken until equilibrium. Additionally, 5.0 to 200 mg L^{-1} Pb^{2+} concentrations were utilized to determine how the Fe_2O_3@Al_2O_3 nanocomposite's Pb^{2+} removal was affected by the starting Pb^{2+} concentration. In addition, sorption at the concentrations noted previously was carried out at 20, 35, and 50 °C to examine the impact of temperature on Pb^{2+} removal. The findings were applied to the study of the thermodynamics and sorption isotherms.

2.5. Regeneration and Sorbent Reusability

A 50 mL sample solution containing Pb^{2+} (60 mg L^{-1}) was placed in a glass bottle with a stopper, and the pH was adjusted to 5 using 0.1 mol L^{-1} HCl and 0.1 mol L^{-1} NaOH. Then, 50 mg of $Fe_2O_3@Al_2O_3$ was added to the bottle. The mixture was shaken at 250 rpm and 25 ± 1 °C for 60 min. The $Fe_2O_3@Al_2O_3$ nanocomposite was separated, and the adsorbed Pb^{2+} ions were tested for desorption using 5 mL of different concentrations of NaEDTA (0.1–0.5 mol L^{-1}). The concentration of the metal ions in the eluent was determined using ICP-AES.

2.6. Application to real samples

Seawater (SW) and groundwater (GW) samples were collected and filtered through a cellulose nitrate membrane (0.45 µm pore size). Then, the samples were acidified with 2% HNO3 and kept in polyethylene bottles at 4 °C until analysis.

3. Results and Discussion

3.1. Characterization

The particle morphology of the sample at a nanometer-scale length was observed using scanning electron microscopy (SEM; Fig. 1a,b). The images show a difference in the overall nanostructure between the host material and the composites. Porous alumina consists of irregularly shaped particles, while the nanocomposite $Fe_2O_3@Al_2O_3$ shows a more compact structure, consisting of smaller particles with a size range of 14.1–20.6 nm. This difference originates from using iron oxide as a precursor in the preparation of nanocomposites because of the seeding effect of iron oxide. The initiation of the transformation in porous alumina requires sufficient energy to overcome the nucleation barrier. In the composite system, iron oxide particles provide nuclei; thus, the nucleation stage is removed, reducing the energy requirement.

The magnetic nanoparticles in the composite materials were studied using transmission electron microscopy (TEM). Figure 1c shows that the magnetic c-Fe_2O_3 nanoparticles divided finely inside the finished material. It is impossible to distinguish between the alumina oxidic structures and iron at the nanometer-scale length. The results indicate that the magnetic nanoparticles in this material are very tiny, in the range of 3.5 to 13.9 nanometers.

Energy dispersive X-ray (EDX) mapping was used to estimate the elements in the fabricated $Fe_2O_3@Al_2O_3$ nanocomposite (Fig. 1d). The aluminum, oxygen, and iron(III) mass percentages in the nanocomposite were 40.28%, 46.65 %, and 13.07%, respectively. According to the results and the good $Fe_2O_3@Al_2O_3$ nanocomposite distribution observed in the SEM images, in addition to the results of the EDX analysis, the formation of the $Fe_2O_3@Al_2O_3$ nanocomposite was established. Furthermore, the EDX mapping corroborated our explanations, and the final results correspond with those obtained from the elemental mapping in Fig. 2, which indicates an excellent homogeneous product.

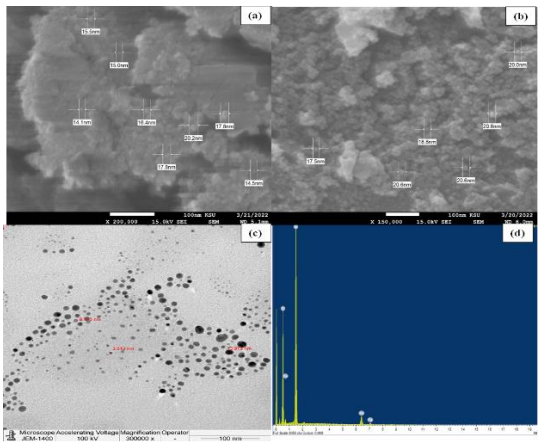

Fig. 1 (a, b) Two spots SEM images (c) TEM, and (d) EDX results of the prepared $Fe_2O_3@Al_2O_3$ nanocomposite**.**

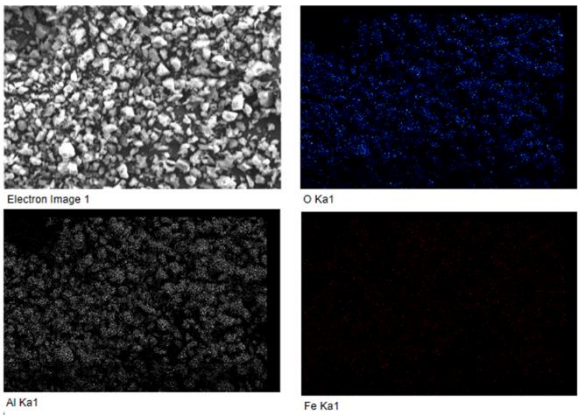

Fig. 2 obtained resulted elemental mapping of Fe, O and Al in the prepared $Fe_2O_3@Al_2O_3$ nanocomposite**.**

The overlapping X-ray diffraction (XRD) patterns of Fe_2O_3, Al_2O_3, and $Fe_2O_3@Al_2O_3$ are presented in Fig. 3. The powder XRD (PXRD) pattern of the $Fe_2O_3@Al_2O_3$ nanocomposite matched the rhombohedral α-Fe_2O_3 (JCPDS 01-1053) and Al2O3 (JCPDS 37-1462) standard results [44-47]. The diffraction pattern for $Fe_2O_3@Al_2O_3$ showed diffraction peaks from both Fe_2O_3 and Al_2O_3, showing that the structures of both materials were retained after compositing at 1000 °C of calcination; the Fe_2O_3 peaks began to appear at this temperature. This proves that iron is present in the nanocomposite, and because Al_2O_3 is amorphous at lower temperatures, the amorphous nature masked the Fe_2O_3. However, as the crystallinity of Al_2O_3 increased at high temperatures, Fe_2O_3 began to appear.

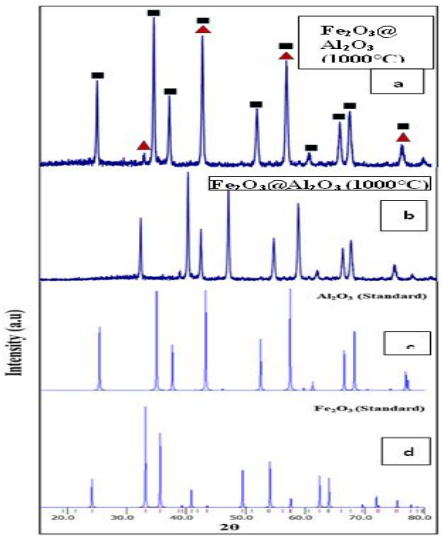

Fig. 3 X-ray diffraction (XRD) patterns of synthesized nanocomposite, Fe_2O_3 and Al_2O_3 standards (▲represents the α- Fe_2O_3 peaks and ■ represents Al_2O_3 peaks).

The FTIR spectra are presented in Fig. 4a for the Fe_2O_3@Al_2O_3 nanocomposite. The most abundant peaks at 738 and 899 cm^{-1} were allocated to Al-O-Al symmetric and asymmetric stretching vibrations, while the band at 586 cm^{-1} was assigned to the Al-O-Al bending vibration and/or Fe-O stretching [48, 49]. The bending band at 560 cm^{-1} may be attributed to the Al-O-Al bending and/or Fe-O stretching vibrations. The broad absorption band at 1348–3200 cm^{-1} can be assigned to the O-H bending and stretching vibrations of the adsorbed moisture [44, 45, 50, 51].

The pore structure and surface area of our sample were established from nitrogen adsorption–desorption isotherm analysis. As seen in Fig. 4b,c, the porous alumina displayed a type H3 hysteresis loop isotherm, characteristic of mesoporous materials; hysteresis was noticed from the occurrence of capillary pore condensation. The type H3 hysteresis loop in the Fe_2O_3@Al_2O_3 nanocomposite was assigned to slit-like non-rigid-aggregate particles with cylindrical micro-pores [52, 53]. The Fe_2O_3@Al_2O_3 nanocomposite had pore diameter (PD), pore volume (PV), and surface area (SA) values of 11.44 nm, 0.37 cm^3 g^{-1}, and 113.46 m^2 g^{-1}, respectively, as determined using the BET equation, indicating a high potential sorption capacity for the Fe_2O_3@Al_2O_3.

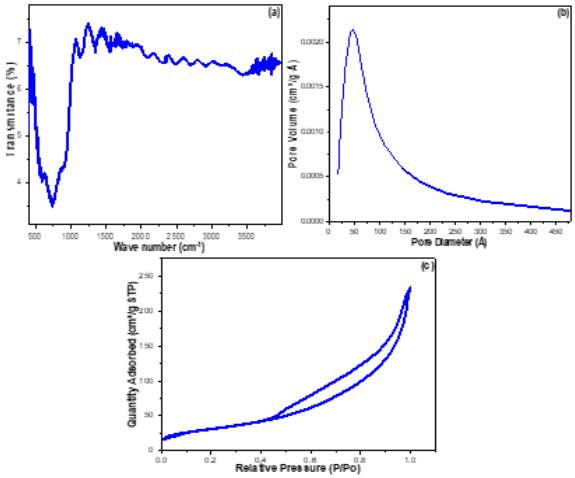

Fig. 4 (a) FTIR findings, (b) the pore size-volume distribution of the Al_2O_3@Fe_2O_3 nanocomposites, and (c) the N_2-adsorption-desorption-isotherm.

3.2. Static adsorptions

3.2.1. Effect of pH on the adsorption of Pb(II)

The pH is a critical parameter in the adsorption and separation of heavy metal ions, as it affects the real-life applications of the nanocomposite. The adsorption of Pb^{2+} ions by the Fe_2O_3@Al_2O_3 nanocomposite is strongly depended on pH of studied solution. Fig. 5a demonstrates that Pb^{2+} sorption increasing progressively as the pH increased and reached its maximum value at pH 5. This is understandable, since the sorbent is protonated at low pH, repelling the positively charged Pb^{2+} ions. The experiment over pH 6 were avoided to prevent the precipitation of Pb^{2+} ions as hydroxides.

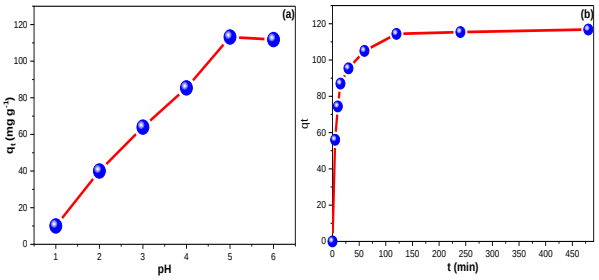

Fig. 5 (a) the pH study for Pb^{2+} removal, and (b) is the contact time study (the concentration of Pb^{2+} is 60 mg L^{-1} and 60 mg Al_2O_3@Fe_2O_3 nanocomposites).

3.2.2. Kinetics

The effect of contact time on the adsorption of Pb^{2+} by Fe_2O_3@Al_2O_3 was studied by changing the shaking time (10–250 min). As shown in Fig 5b, the adsorption of Pb^{2+} onto the Fe_2O_3@Al_2O_3 nanocomposite occurs in two phases. The first phase is instantaneous external surface adsorption, while the second phase is slower diffusion-controlled adsorption. With increasing contact time, the

Fe_2O_3@Al_2O_3 nanocomposite surface was filled, and the adsorption rate slowed and stabilized.

From the figures, it can be observed that the adsorption peaked after almost 60 min. This behaviour is due to the large number of adsorption sites available for Pb^{2+} adsorption; equilibrium was attained once the adsorption sites were all occupied. The sorption rate was investigated using pseudo-first-order (PFO) and pseudo-second-order (PSO) kinetic models (Eqs. (2) and (3)), and the intra-particle and liquid-film diffusion models (IPM and LFM) were used to determine the mechanism regulating adsorption (Eqs. (4) and (5)) [55]. The graphs were used to determine the rate constants. The parameters associated with the kinetics are reported in Table 1. According to the results, the adsorption of Pb^{2+} onto Fe_2O_3@Al_2O_3 was best characterized via the pseudo-second-order model, because its correlation coefficient (R^2) was nearest to 1, and the value of the determined adsorption capacity (qe,cal) was lower than the experimental one (qe,exp). Other factors controlled the adsorption rate; the mechanism was investigated utilizing the LFM and IPM. Table 1 shows that the liquid-film diffusion controlled the Pb^{2+} removal. These findings imply a high affinity of Pb^{2+} for the Fe_2O_3@Al_2O_3 [54-56].

Even though the adsorption equilibrium was not attained until 4 h later, almost 90% of the total uptake occurred in the first 1 h. Fe_2O_3@Al_2O_3 possessed a qt value of 116.8 mg g^{-1} for removing Pb^{2+} from the studied sample. This finding aligned with the amorphous morphology revealed by SEM and the SA presented by the BET analysis.

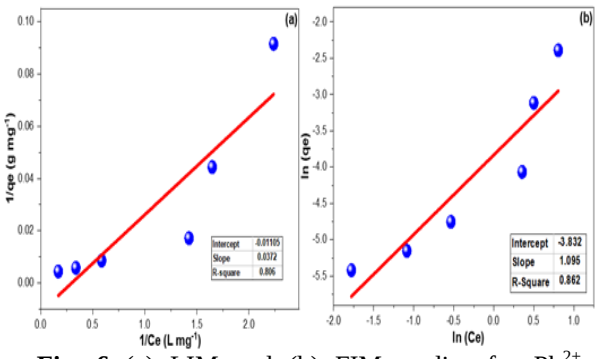

Fig. 6 (a) LIM and (b) FIM studies for Pb^{2+} adsorption on Al_2O_3@Fe_2O_3 nanocomposite at 20°C from 5 to 100 mg L^{-1} Pb^{2+} solutions

Table 1 The kinetic results of Pb^{2+} adsorption onto the Al_2O_3@Fe_2O_3 nanocomposite.

Adsorption rate order						
q_e exp. (mg g^{-1})	PFO			PSO		
	q_e cal. (mg g^{-1})	R^2	k_1 ($_{L^{-1}}^{mg}$)	q_e cal. (mg g^{-1})	R^2	k_2 (g mg^{-1} min^{-1})
116.800	38.917	0.89	0.026	21.335	1.00	0.256
Adsorption rate control mechanism						
IPM			LFM			
KIP (mg g^{-1} $min^{-0.5}$)	C (mg g^{-1})	R^2	KLF (min^{-1})	R^2		
3.965	64.791	0.758	0.016	0.887		

3.2.3. Adsorption equilibrium isotherms

Adsorption isotherms were vital to the current investigation, as they explain the interactive behaviour between the adsorbent and adsorbate. The results for the effect of concentration were used to analyze the adsorption isotherms. The monolayer and multilayer adsorption potentials were investigated using the Langmuir and Freundlich isotherm models (LIM and FIM) given in Eqs. 6 and 7, respectively [57, 58].

$$\frac{1}{q_e} = \frac{1}{K_L\, q_m} . \frac{1}{C_e} + \frac{1}{K_L} \quad (6)$$

$$\ln q_e = \ln K_F + \frac{1}{n} \ln C_e \quad (7)$$

where K_L (L mg^{-1}) is the LIM constant; C_e (mg L^{-1}) is the equilibrium solution concentration; q_m (mg g^{-1}) is the computed maximum qt value; and KF (L mg^{-1}) and 1/n (arbitrary) denote the FIM equilibrium constant and heterogeneity factor, respectively [59].

There are four assumptions for the Langmuir isotherm model: (i) the interaction forces between the absorbed molecules are not significant; (ii) once the adsorption sites are occupied, no more adsorption occurs; (iii) at specific egalitarian adsorption sites inside the adsorbent, adsorption increases; and (iv) the intermolecular forces of attraction reduce rapidly with distance. Table 2 indicates the correlation coefficients and Langmuir constants for the nanocomposite determined from the graph of 1/qe against $1/C_e$ (Figure 6). The experimental results corresponded with the Langmuir model at 20 °C (atmosphere temperature).

An indeterminate constant separation factor, RL, was determined to decide whether the Langmuir-type adsorption process was favourable. The isotherm patterns were unfavourable, favourable, irreversible, and linear for RL > 1, RL < 1, RL = 0, and RL = 1, respectively. RL can be expressed computationally as follows [61]:

$$Rl = \frac{1}{1+Kl\ Co} \quad (8)$$

where K_L represents the Langmuir constant (L mg^{-1}), and Co represents the initial Pb^{2+} concentration (mg L^{-1}).

The empirical isotherm utilized for the multiple-layer adsorption was the Freundlich isotherm. The constants of Freundlich, n and KF determined from the graph of ln q_e against ln Ce (Figure 6) are given in Table 2. For a larger value of KF, the capacity is greater [62]. The value of n was more than 1 (n > 1), demonstrating that the Freundlich adsorption type was favourable and the Pb^{2+} adsorption on Fe_2O_3@Al_2O_3 fit the FIM.

Table 2 Isotherms and thermodynamic findings of Pb^{2+} adsorption onto the Al_2O_3@Fe_2O_3 nanocomposite

Adsorption isotherms					
Langmuir			Freundlich		
R^2 (a.u.)	K_L (L mg^{-1})	q_m (mg g^{-1})	R^2 (a.u.)	K_f (L mg^{-1})	n^{-1} (a.u.)
0.806	-483.545	-0.095	0.862	0.018	0.896
Thermodynamic parameters					
Fed conc. (mg L^{-1})	ΔH◦ (kJmol^{-1})	ΔS◦ (kJmol^{-1})	ΔG° (kJmol^{-1}) 298 K	ΔG◦ (kJmol^{-1}) 308 K	ΔG◦ (kJmol^{-1}) 318 K
5.0	187.662	0.643	-4.067	-10.501	-16.935
10.0	83.205	0.283	-1.154	-3.984	-6.815
25.0	66.264	0.250	-8.327	-10.830	-6.815
50.0	19.451	0.093	-8.226	-9.155	-10.084
75.0	32.978	0.138	-8.026	-9.402	-10.778
100.0	52.120	0.199	-7.036	-9.021	-11.006

3.2.4. Thermodynamic

The effect of temperature on Pb^{2+} removal by Fe_2O_3@Al_2O_3 is shown in Fig. 7a. Noteworthily, at 40 °C, Fe_2O_3@Al_2O_3 exhibited an experimental qt of 246.4 mg g^{-1} from 100 mg L^{-1}. Since qt values were proportional to temperature, the positive ΔH^o showed that the process was endothermic. Next, the Pb^{2+} sorption on the Fe_2O_3@Al_2O_3 nanocomposite was investigated from a thermodynamic standpoint (Fig. 7b). Table 2 displays the results of applying Eq. 9 to compute the enthalpy (ΔH^o) and entropy (ΔS^o), and then using Eq. 10 to calculate the Gibbs free energy (ΔG^o), where T is the temperature in kelvin and K is an equilibrium constant related to the Langmuir constant.

$$\ln K_c = \frac{\Delta H^o}{RT} + \frac{\Delta S^o}{R} \quad (9)$$

$$\Delta G^o = \Delta H^o - T\Delta S^o \quad (10)$$

The temperature of the solution was varied to explore the effect of temperature on the adsorption process. The influence of the solution temperature on adsorption is complicated due to the following three effects [63] of increasing the solution temperature: (i) an increased diffusion rate (positive effect on adsorption); (ii) increased solubility decreasing the hydrophobic features of the adsorbates (negative effect on adsorption); (iii) increased vibrational energy of the adsorbates, stimulating the desorption of adsorbates (negative effect on adsorption).

The ideal gas constant was set at 0.0081345 kJ mol^{-1} (R). The earlier endothermic hypothesis was backed up by the positive ΔH^o values. Furthermore, the Pb^{2+} sorption on the Fe_2O_3@Al_2O_3 nanocomposite was spontaneous, as evidenced by the negative ΔG^o values. Additionally, the ΔG^o values were all <20 kJ mol^{-1}, suggesting physisorption occurred [27]. The resulted adsorption capacity of Pb^{2+} onto Fe_2O_3@Al_2O_3 nanocomposite (q_t 246.4 mg g^{-1}) confirm that the fabricated Fe_2O_3@Al_2O_3 sorbent used in this study is competitive to those found in previous literatures (Table 4).

Table 4 Comparing the adsorption capacity of Al_2O_3@Fe_2O_3 nanocomposite with previously reported sorbents found in the literature.

Sorbents	**Adsorption capacity mg g^{-1}**	**Ref**
Al_2O_3@Fe_2O_3	**246.4**	**This study**
dolomite-quartz@Fe_3O_4	71.42	[60]
PPy/Fe_3O_4	11.35	[61]
Fe_2O_3–Al_2O_3	23.75	[62]
CDs/Al_2O_3	177. 83	[63]
PANI-Al_2O_3	9.90	[64]
Polyaniline/Fe_3O_4	111.11	[65]

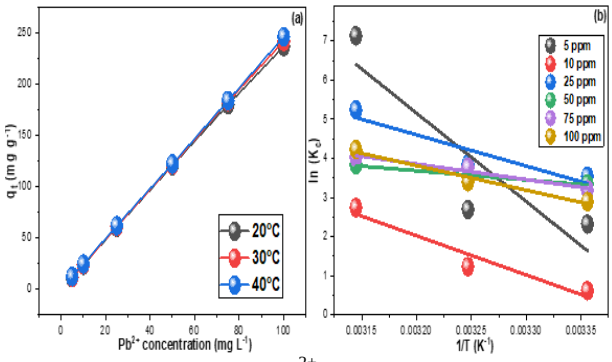

Fig. 7 (a) the effect of Pb^{2+} initial concentration (5, 10, 25, 50, 75, and 100 ppm) on its sorption by the Fe_2O_3@Al_2O_3 at 20, 30, and 40°C; (b) thermodynamic investigation of Pb2+ sorption by Fe_2O_3@Al_2O_3 from 5 to 100 mg L-1 solutions at 20, 30, and 40°C.

3.2.5. Regeneration and Reusability of Fe_2O_3@Al_2O_3

The Fe_2O_3@Al_2O_3 nanocomposite regeneration was tested after loading the nanocomposite with the maximum capacity of Pb^{2+} ions. Different concentrations of Na_2EDTA (0.1–0.5 mol L^{-1}) were tested as eluent for the regeneration process, and the experiment was performed by changing the eluent concentration while keeping all other parameters constant. Na_2EDTA (0.4-0.5 mol L^{-1}) resulted in the

best $Fe_2O_3@Al_2O_3$ regeneration, and the elution efficiency reached ≈ 98.5%. Over at least three cycles, no appreciable loss in $Fe_2O_3@Al_2O_3$ activity was observed. To examine the reusability of $Fe_2O_3@Al_2O_3$, four repeated adsorption–desorption cycles were performed under the previously determined optimal conditions. The results are presented in Table 3. The adsorption efficiency of the $Fe_2O_3@Al_2O_3$ nanocomposite showed no significant decrease. After the fourth experiment, the sorbent activity was 94.2% of its original efficiency, with an RSD of 5.19.

Table 3 The Reusability study of 10 mg of $Al_2O_3@Fe_2O_3$ in treating 25 mL of solution containing 60 mg L^{-1} Pb^{2+} , pH 5, shaking time 120 min.

No of cycles	Recovery % of $\mathbf{Pb^{+2}}$
1	99.2
2	97.8
3	96.5
4	94.2

3.2.6. Application

Figure 8b tracks the outcomes of removing Pb^{2+} from polluted GW and SW using the synthesized nanocomposite. $Fe_2O_3@Al_2O_3$ showed an average efficiency of 96.8% in treated SW and GW samples containing 5.0 and 10.0 mg L^{-1} Pb^{2+} concentrations, with an RSD% value of 1.045. SW polluted with 10.0 mg L^{-1} Pb^{2+} yielded a lower separation efficiency, possibly due to the high saline concentration, which impedes Pb^{2+} transport.

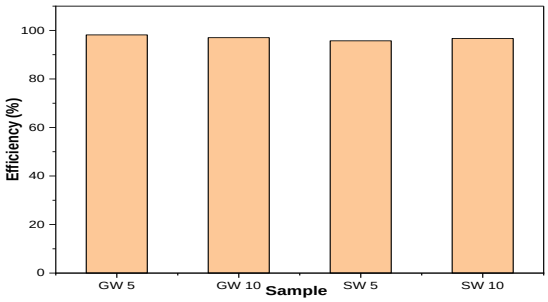

Fig. 8, Removal of Pb^{2+} from groundwater and seawater samples by the prepared $Fe_2O_3@Al_2O_3$.

4. Conclusions

$Fe_2O_3@Al_2O_3$ was prepared via a facile, fast method, employing GL for capping purposes.

It is worth mentioning that the 22.41 g of $AlCl_3.6H_2O$, 1.13 g of $FeCl_3.6H_2O$, and 10.0 g of GL used to produce 10.0 g of $Fe_2O_3@Al_2O_3$ cost only about 2.0 US dollars, reflecting another of an economic advantage of this simple green method.

The TEM results for the synthesized $Fe_2O_3@Al_2O_3$ revealed a particle size ranging between 3.5 and 13.9 nm. The sorbent possessed a specific surface area of 113.46 m^2 g^{-1}, so it was tested for removing heavy metals from water, using Pb^{2+} as an example. $Fe_2O_3@Al_2O_3$ was proven to be excellent at removing Pb^{2+}, with a q_t value of 246.4 mg g^{-1}. The Pb^{2+} removal fits a PSO model, and the sorption was controlled via LFM. The equilibrium studies revealed a better agreement of Pb^{2+} sorption with the Freundlich isotherm model, while the thermodynamic results implied a spontaneous endothermic physisorption. The $Fe_2O_3@Al_2O_3$ showed an average efficiency of 96.8% in treated SW and GW spiked with Pb^{2+}, and the sorbent activity was 94.2% of its original efficiency, with an RSD of 5.19.

5. References

[1] Elamin, M.R., et al., *Spontaneous Adsorption and Efficient Photodegradation of Indigo Carmine under Visible Light by Bismuth Oxyiodide Nanoparticles Fabricated Entirely at Room Temperature.* 2022. **10**(5): p. 65.

[2] Rahbar-Shamskar, K., et al., *Synthesis of micro/mesoporous carbon adsorbents by in-situ fast pyrolysis of reed for recovering gasoline vapor.* 2020. **259**: p. 120832.

[3] Silva, A.R., et al., *Detoxification of ciprofloxacin in an anaerobic bioprocess supplemented with magnetic carbon nanotubes: Contribution of adsorption and biodegradation mechanisms.* 2021. **22**(6): p. 2932.

[4] Bożęcka, A., M. Orlof-Naturalna, and M.J.J.o.E.E. Kopeć, *Methods of dyes removal from aqueous environment.* 2021. **22**(9).

[5] Ho, S.J.J.o.G. and E. Protection, *Removal of Dyes from Wastewater by Adsorption onto Activated Carbon: Mini Review.* 2020. **8**(05): p. 120.

[6] Sivaprakasha, S., P.S. Kumarb, and S.J.I.J.o.A.C. Krishnac, *Adsorption study of various dyes on Activated Carbon Fe3O4 Magnetic Nano Composite.* 2017. **13**(2): p. 255-266.

[7] Fiyadh, S.S., et al., *The modelling of lead removal from water by deep eutectic solvents functionalized CNTs: artificial neural network (ANN) approach.* Water Science and Technology, 2017. **76**(9): p. 2413-2426.

[8] Vesali-Naseh, M., M.R.V. Naseh, and P. Ameri, *Adsorption of Pb (II) ions from aqueous solutions using carbon nanotubes: A systematic review.* Journal of Cleaner Production, 2021. **291**: p. 125917.

[9] Rasoulzadeh, H., et al., *Parametric modelling of Pb (II) adsorption onto chitosan-coated Fe3O4 particles through RSM and DE hybrid evolutionary optimization framework.* Journal of Molecular Liquids, 2020. **297**: p. 111893.

[10] Farooq, U., et al., *Biosorption of heavy metal ions using wheat based biosorbents–a review of the recent literature.* Bioresource technology, 2010. **101**(14): p. 5043-5053.
[11] Zuo, Q., et al., *Preparation of activated carbon fibers rich in S/N/O adsorption sites for selective and efficient trace Pb (II) removal from drinking water.* Process Safety and Environmental Protection, 2022. **166**: p. 113-122.
[12] Vuković, G.D., et al., *Removal of lead from water by amino modified multi-walled carbon nanotubes.* Chemical Engineering Journal, 2011. **173**(3): p. 855-865.
[13] Labiadh, L., et al., *Direct and indirect electrochemical oxidation of Indigo Carmine using PbO2 and TiRuSnO2.* Journal of Solid State Electrochemistry, 2017. **21**(8): p. 2167-2175.
[14] Ullah, F., et al., *Classification, processing and application of hydrogels: A review.* Materials Science and Engineering: C, 2015. **57**: p. 414-433.
[15] Gemeay, A.H., E.F. Aboelfetoh, and R.G. El-Sharkawy, *Immobilization of green synthesized silver nanoparticles onto amino-functionalized silica and their application for indigo carmine dye removal.* Water, Air, & Soil Pollution, 2018. **229**(1): p. 1-17.
[16] Emik, S., S. Işık, and E. Yıldırım, *Simultaneous removal of cationic and anionic dyes from binary solutions using carboxymethyl chitosan based IPN Type resin.* Journal of Polymers and the Environment, 2021. **29**(6): p. 1963-1977.
[17] Zein, R., et al., *The improvement of indigo carmine dye adsorption by Terminalia catappa shell modified with broiler egg white.* Biomass Conversion and Biorefinery, 2022: p. 1-18.
[18] Topare, N.S. and S.A. Bokil, *Adsorption of textile industry effluent in a fixed bed column using activated carbon prepared from agro-waste materials.* Materials Today: Proceedings, 2021.
[19] Yurtsever, A., et al., *Self-forming dynamic membrane bioreactor for textile industry wastewater treatment.* Science of The Total Environment, 2021. **751**: p. 141572.
[20] Feng, Q., et al., *Flocculation performance of papermaking sludge-based flocculants in different dye wastewater treatment: Comparison with commercial lignin and coagulants.* Chemosphere, 2021. **262**: p. 128416.
[21] Othman, M.H.D., et al., *Advanced Membrane Technology for Textile Wastewater Treatment*, in *Membrane Technology Enhancement for Environmental Protection and Sustainable Industrial Growth*. 2021, Springer. p. 91-108.
[22] Ahsan, M.A., et al., *Carbonization of Co-BDC MOF results in magnetic C@ Co nanoparticles that catalyze the reduction of methyl orange and 4-nitrophenol in water.* Journal of Molecular Liquids, 2019. **290**: p. 111059.
[23] Ahsan, M.A., et al., *Fe nanoparticles encapsulated in MOF-derived carbon for the reduction of 4-nitrophenol and methyl orange in water.* Catalysis Communications, 2019. **130**: p. 105753.
[24] Ahsan, M.A., et al., *Ultrafast catalytic reduction of environmental pollutants in water via MOF-derived magnetic Ni and Cu nanoparticles encapsulated in porous carbon.* Applied Surface Science, 2019. **497**: p. 143608.
[25] Almufarij, R.S., et al., *Optimization, Nature, and Mechanism Investigations for the Adsorption of Ciprofloxacin and Malachite Green onto Carbon Nanoparticles Derived from Low-Cost Precursor via a Green Route.* 2022. **27**(14): p. 4577.
[26] Ghoniem, M.G., et al., *Highly selective removal of cationic dyes from wastewater by MgO nanorods.* 2022. **12**(6): p. 1023.
[27] Elamin, M.R., et al., *Linear and nonlinear investigations for the adsorption of paracetamol and metformin from water on acid-treated clay.* 2021. **11**(1): p. 1-13.
[28] Elamin, M.R., B.Y. Abdulkhair, and A.O.J.S.r. Elzupir, *Insight to aspirin sorption behavior on carbon nanotubes from aqueous solution: Thermodynamics, kinetics, influence of functionalization and solution parameters.* 2019. **9**(1): p. 1-10.
[29] Abdulkhair, B., et al., *Adsorption behavior of barium ions onto ZnO surfaces: Experiments associated with DFT calculations.* Journal of Molecular Structure, 2021. **1223**: p. 128991.
[30] Prins, R.J.J.o.C., *On the structure of γ-Al2O3.* 2020. **392**: p. 336-346.
[31] Gao, X., et al., *Anti-coking and anti-sintering Ni/Al2O3 catalysts in the dry reforming of methane: recent progress and prospects.* 2021. **11**(8): p. 1003.
[32] Cui, K., et al., *Effects of Cr2O3 content on microstructure and mechanical properties of Al2O3 matrix composites.* 2021. **11**(2): p. 234.
[33] Khan, M., et al., *Electro-oxidation of ammonia at novel Ag2O− PrO2/γ-Al2O3 catalysts.* 2021. **11**(2): p. 257.
[34] Khan, S., et al., *Electro-oxidation of ammonia over copper oxide impregnated γ-Al2O3 nanocatalysts.* 2021. **11**(3): p. 313.
[35] Yeşiltepe Özcelik, D., et al., *Mixed oxides NiO/ZnO/Al2O3 synthesized in a single step via ultrasonic spray pyrolysis (USP) method.* 2022. **12**(1): p. 73.
[36] Elsayed, A.M., et al., *Preparation of hexagonal nanoporous Al2O3/TiO2/TiN as a novel photodetector with high efficiency.* 2021. **11**(1): p. 1-12.

[37] Zhukovskii, Y.F., et al., *Doped 1D Nanostructures of Transition-metal Oxides: First-principles Evaluation of Photocatalytic Suitability.* 2017. **57**(6): p. 461-476.
[38] Sui, R., et al., *Improved carbon disulfide conversion: Modification of an alumina Claus catalyst by deposition of transition metal oxides.* Applied Catalysis A: General, 2020. **604**: p. 117773.
[39] Pradier, C., et al., *Supported chromia catalysts for oxidation of organic compounds: the state of chromia phase and catalytic performance.* Applied Catalysis B: Environmental, 2000. **27**(2): p. 73-85.
[40] Adam, F.A., *Influence of Doping-Ion-Type on the Characteristics of Al2O3-Based Nanocomposites and Their Capabilities of Removing Indigo Carmine from Water*. Inorganics, 2022. **10**(9): p. 144.
[41] Khraisheh, M., M.A. Al-Ghouti, and C.A. Stanford, *The application of iron coated activated alumina, ferric oxihydroxide and granular activated carbon in removing humic substances from water and wastewater: Column studies.* Chemical Engineering Journal, 2010. **161**(1-2): p. 114-121.
[42] Sun, W., et al., *Preparation of Cu-Ce@ γ-Al2O3 and Study on Catalytic Ozone Oxidation for the Treatment of RO Concentrate Water*. Water, 2022. **14**(18): p. 2881.
[43] Kamarehie, B., et al., *Catalytic ozonation process using PAC/γ-Fe2O3 to Alizarin Red S degradation from aqueous solutions: a batch study*. Chemical Engineering Communications, 2019. **206**(7): p. 898-908.
[44] Guivar, J.A.R., et al., *Vacancy ordered γ-Fe2O3 nanoparticles functionalized with nanohydroxyapatite: XRD, FTIR, TEM, XPS and Mössbauer studies.* Applied Surface Science, 2016. **389**: p. 721-734.
[45] Padil, V.V.T. and M.J.I.j.o.n. Černík, *Green synthesis of copper oxide nanoparticles using gum karaya as a biotemplate and their antibacterial application.* 2013. **8**: p. 889.
[46] Rajeswari, V.D., et al., *Green and ecofriendly synthesis of cobalt oxide nanoparticles using Phoenix dactylifera L: antimicrobial and photocatalytic activity*. 2021: p. 1-9.
[47] Dharmaraj, N., et al., *Synthesis of nickel oxide nanoparticles using nickel acetate and poly (vinyl acetate) precursor*. 2006. **128**(1-3): p. 111-114.
[48]Afkhami, A., M. Saber-Tehrani, and H. Bagheri, *Simultaneous removal of heavy-metal ions in wastewater samples using nano-alumina modified with 2, 4-dinitrophenylhydrazine*. Journal of hazardous materials, 2010. **181**(1-3): p. 836-844.
[49] Prabhakar, R. and S. Samadder, *Low cost and easy synthesis of aluminium oxide nanoparticles for arsenite removal from groundwater: a complete batch study*. Journal of Molecular Liquids, 2018. **250**: p. 192-201.
[50] Afkhami, A., M. Saber-Tehrani, and H.J.J.o.h.m. Bagheri, *Simultaneous removal of heavy-metal ions in wastewater samples using nano-alumina modified with 2, 4-dinitrophenylhydrazine.* 2010. **181**(1-3): p. 836-844.
[51] Prabhakar, R. and S.J.J.o.M.L. Samadder, *Low cost and easy synthesis of aluminium oxide nanoparticles for arsenite removal from groundwater: a complete batch study.* 2018. **250**: p. 192-201.
[52] Sun, S., et al., *Microstructural investigation of gas shale in Longmaxi formation, Lower Silurian, NE Sichuan basin, China.* 2017. **35**(4): p. 406-429.
[53] Thommes, M., et al., *Physisorption of gases, with special reference to the evaluation of surface area and pore size distribution (IUPAC Technical Report).* 2015. **87**(9-10): p. 1051-1069.
[54] Elamin, M.R., B.Y. Abdulkhair, and A.O. Elzupir, *Removal of ciprofloxacin and indigo carmine from water by carbon nanotubes fabricated from a low-cost precursor: Solution parameters and recyclability.* Ain Shams Engineering Journal, 2023. **14**(1): p. 101844.
[55] Almufarij, R.S., et al., *Sweep-Out of Tigecycline, Chlortetracycline, Oxytetracycline, and Doxycycline from Water by Carbon Nanoparticles Derived from Tissue Waste.* Nanomaterials, 2022. **12**(20): p. 3617.
[56] Almufarij, R.S., et al., *Optimization, Nature, and Mechanism Investigations for the Adsorption of Ciprofloxacin and Malachite Green onto Carbon Nanoparticles Derived from Low-Cost Precursor via a Green Route.* Molecules, 2022. **27**(14): p. 4577.
[57] Elamin, M.R., B.Y. Abdulkhair, and A.O. Elzupir, *Insight to aspirin sorption behavior on carbon nanotubes from aqueous solution: Thermodynamics, kinetics, influence of functionalization and solution parameters.* Scientific reports, 2019. **9**(1): p. 1-10.
[58] Elamin, M.R., A.O. Elzupir, and B.Y. Abdulkhair, *Synthesis and characterization of functionalized carbon nanofibers for efficient removal of highly water-soluble dextromethorphan and guaifenesin from environmental water samples.* Environmental Nanotechnology, Monitoring & Management, 2021. **15**: p. 100397.
[59] Elamin, M.R., et al., *Spontaneous Adsorption and Efficient Photodegradation of Indigo Carmine under Visible Light by Bismuth Oxyiodide Nanoparticles Fabricated Entirely at Room Temperature.* Inorganics, 2022. **10**(5): p. 65.
[60] El Mouden, A., et al., *Removal of cadmium and lead ions from aqueous solutions by novel dolomite-quartz@ Fe3O4 nanocomposite fabricated as nanoadsorbent.* Environmental Research, 2023. **225**: p. 115606.
[61] Foroutan, R., et al., *Cadmium ion removal from aqueous media using banana peel*

biochar/Fe3O4/ZIF-67. Environmental Research, 2022. **211**: p. 113020.
[62] Mahapatra, A., B. Mishra, and G. Hota, *Electrospun Fe2O3–Al2O3 nanocomposite fibers as efficient adsorbent for removal of heavy metal ions from aqueous solution.* Journal of hazardous Materials, 2013. **258**: p. 116-123.
[63] Fouda-Mbanga, B., E. Prabakaran, and K. Pillay, *Synthesis and characterization of CDs/Al2O3 nanofibers nanocomposite for Pb2+ ions adsorption and reuse for latent fingerprint detection.* Arabian Journal of Chemistry, 2020. **13**(8): p. 6762-6781.
[64] Joshi, N.C. and S. Negi, *Synthesis and adsorption potential of an organic–inorganic-based hybrid nanomaterial (PANI-Al2O3).* Inorganic and Nano-Metal Chemistry, 2022. **52**(3): p. 451-460.
[65] Sadeghi, M.M., et al., *Preparation of magnetic nanocomposite based on polyaniline/Fe3O4 towards removal of lead (II) ions from real samples.* Synthetic Metals, 2018. **245**: p. 1-9.